AGU PUBLICATIONS

JGR

Journal of Geophysical Research: Biogeosciences

RESEARCH ARTICLE
10.1002/2014JG002764

Key Points:
- Neutrophilic FeOB exert a significant role in forming the Fe-rich oxyhydroxides
- FeOB could be a tempting explanation for the existence of BIFs
- Our results have a significant implication for the formation of ancient BIFs

Supporting Information:
- Readme
- Figures S1–S4 and Table S1

Correspondence to:
J. Li,
lijiwei20025@sidsse.ac.cn

Citation:
Sun, Z., J. Li, W. Huang, H. Dong, C. T. S. Little, and J. Li (2015), Generation of hydrothermal Fe-Si oxyhydroxide deposit on the Southwest Indian Ridge and its implication for the origin of ancient banded iron formations, *J. Geophys. Res. Biogeosci.*, *120*, 187–203, doi:10.1002/2014JG002764.

Received 2 AUG 2014
Accepted 27 DEC 2014
Accepted article online 7 JAN 2015
Published online 30 JAN 2015

Generation of hydrothermal Fe-Si oxyhydroxide deposit on the Southwest Indian Ridge and its implication for the origin of ancient banded iron formations

Zhilei Sun[1,2], Jun Li[1,2], Wei Huang[1,2], Hailiang Dong[3], Crispin T. S. Little[4], and Jiwei Li[5]

[1]Key Laboratory of Marine Hydrocarbon Resources and Environmental Geology, Ministry of Land and Resources, Qingdao, China, [2]Qingdao Institute of Marine Geology, Qingdao, China, [3]Department of Geology and Environmental Earth Science, Miami University, Oxford, Ohio, USA, [4]School of Earth and Environment, University of Leeds, Leeds, UK, [5]Sanya Institute of Deep-Sea Science and Engineering, Chinese Academy of Sciences, Sanya, China

Abstract Modern hydrothermal Fe-Si oxyhydroxide deposits are now known to be analogues to ancient siliceous iron formations. In this study, samples of Fe-Si oxyhydroxide deposits were collected from hydrothermal field on the Southwest Indian Ridge. An investigation of mineralization in these deposits was carried out based on a series of mineralogical and morphological methods. X-ray diffraction and selected area electron diffraction analysis show that amorphous opal and poorly crystalline ferrihydrite are the major minerals. Furthermore, some typical filament structures detected by scanning electronic microscopy examinations, probably indicating the presence of Fe-oxidizing bacteria (FeOB), are pervasive with the main constituents being Fe, Si, P, and C. We thus believe that chemolithoautotrophic FeOB play a significant role in the formation of Fe oxyhydroxide which can effectively oxidize reduced Fe(II) sourced from hydrothermal fluids. Precipitation of amorphous silica, in contrast, is only a passive process with the Fe oxyhydroxide acting as a template. The distinct microlaminae structure alternating between the Fe-rich and Si-rich bands was observed in our samples for the first time in modern seafloor hydrothermal systems. We propose that its formation was due to the episodic temperature variation of the hydrothermal fluid which controls the biogenic Fe oxyhydroxide formation and passive precipitation of silica in this system. Our results might provide a clue for the formation mechanism of ancient banded iron formations.

1. Introduction

Pervasive Fe-Si oxyhydroxide deposits have been commonly found on the modern marine hydrothermal fields from various geological setting such as mid-ocean ridges [e.g., *Kennedy et al*., 2003a, 2003b; *Hrischeva and Scott*, 2007; *Toner et al*., 2009; *Dekov et al*., 2009; *Sun et al*., 2012], seamounts [e.g., *Dekov et al*., 2009; *Edwards et al*., 2011], and back-arc spreading centers [e.g., *Dekov and Savelli*, 2004; *Kato et al*., 2009]. Their special mineralogical assemblage and morphological characteristics invoke increasing interests to investigate the interaction between microbes and minerals and fluids in this marine extreme environment. At present, there is increasing evidence indicating that chemolithoautotrophic FeOB are considered to be the key factor in the formation of Fe-rich oxyhydroxide deposits [e.g., *Emerson and Moyer*, 2002; *Kennedy et al*., 2003a, 2003b, 2004; *Emerson et al*., 2010; *Chan et al*., 2011]. However, the concrete role of FeOB, whether just completely passive or more facilitated activity, played in this process needs to be further clarified.

Furthermore, modern hydrothermal Fe-Si oxyhydroxide deposits in the seafloor are generally considered to be the analogues of ancient Fe- and Si-rich deposits, especially the Precambrian and Paleoproterozoic banded iron formations [*Brown et al*., 1995; *Boyd and Scott*, 2001; *Grenne and Slack*, 2003; *Pecoits et al*., 2009; *Parenteau and Cady*, 2010; *Sun et al*., 2013; *Fru et al*., 2013], whose formation mechanism are still controversial. Specifically, anoxygenic phototrophic bacteria have been considered to play a significant role in the formation of Fe oxides in banded iron formations (BIFs) [e.g., *Widdel et al*., 1993]. However, the possibility that FeOB can also act as an important role in this process has been raised and still needs more evidence to prove [*Cloud*, 1973; *Holm*, 1987a, 1987b; *Kappler et al*., 2005; *Posth et al*., 2008]. In addition, the explanation of the physical separation of the Fe oxides from silica remains to be a major problem of any precipitation model [*Morris*, 1993]. In view of their comparable mineralogical characteristics, cross layer

structure, and formation environment, modern hydrothermal deposit is significant for the interpretation of the formation of BIFs.

The first hydrothermal field at ultraslow spreading Southwest Indian Ridge (SWIR) was discovered during the Chinese DY115-20 expedition in 2008 [*Tao et al*., 2007]. The sulfide chimneys, Fe-rich hydrothermal deposits, and altered basalts have been found to be pervasive in this hydrothermal field [*Zhu et al*., 2010]. *Peng et al.* [2011] take a first to report a high diversity of biogenic Fe-Si oxides (and Fe sulfides) in this hydrothermal field. They proposed that microbes were intricately involved in the formation of the low-temperature deposits in this area. *Li et al.* [2013] further reported a molecular phylogenetic analysis indicating a significant portion of prokaryotes with S, Fe, and Mn metabolism presented in these low-temperature hydrothermal environments. Those data gave some significant implications about the formation of these biogenic minerals in the hydrothermal environment at the SWIR.

However, the role of FeOB in the deposition of Fe-oxides in the low-temperature hydrothermal fluid was not yet addressed completely. Moreover, in our primary investigation based on the Fe-Si-rich hydrothermal deposits, we fortunately observed the distinct microlayer structure alternating between the Fe-rich and Si-rich bands presented for the first time in this newly discovered hydrothermal field on the SWIR. This phenomenon of mineral stratification is highly comparable with ancient Fe-Si formations. We thus herein report on the microtexture, mineralogical, and geochemical compositions in hydrothermal Fe-Si oxyhydroxide deposition the SWIR. Our overarching goal is to further investigate the role of FeOB in the formation of this deposit and draw an ideal generation model for the distinct alternated microlaminae between Fe-rich band and Si-rich band therein. The result of this study would shed new light on the formation mechanism of ancient BIFs.

2. Geological Setting

The SWIR extends ~8000 km from the Bouvet triple junction in the west to the Rodrigues triple junction in the east. It is among the world's slowest spreading ridges with a full spreading rate of about 13–16 mm/yr along most of its length [*Georgen et al*., 2001]. The ridge axis of SWIR is offset by sets of north-south trending transform faults and is characterized by deep axial valleys and low magmatic budget [*Muller et al*., 1999]. The crust of SWIR is about 4 km thick and much thinner than the average thickness of the ocean crust (about 7 km [*Baker and German*, 2004]). The plagioclase-hosted and olivine-hosted melt inclusions from the sections between 70°E and 49°E on the SWIR indicate the high melting fractions of mantle, shallow ridge axis depth, and thick crust [*Font et al*., 2007]. *Cannat et al.* [1999] have identified three types of seafloor at the SWIR as volcanic seafloor, smooth seafloor, and corrugated seafloor.

Evidence for the presence of hydrothermal activity on the SWIR was first reported during the French-UK-Japanese InterRidge cruise in 1997 at several locations between 58.2° and 65.8°E [*German and Parson*, 1998]. Further evidence for additional hydrothermal plumes along the western SWIR and recovery of inactive sulfide deposits and/or metalliferous sediments from both the eastern and western SWIR subsequently followed in subsequent years [*Fujimoto et al*., 1999; *Münch et al*., 2001; *Bach et al*., 2002; *German*, 2003]. However, hydrothermal activity was only confirmed visually during the second China Ocean Mineral Resources Research and Development Association (COMRA) cruise (DY115-19) in 2007 [*Tao et al*., 2007]. Later, in 2008 and 2009, several new hydrothermal fields were discovered along the SWIR during the COMRA cruise (DY115-20 [*Chen and Li*, 2009]).

The samples used in this study were recovered from one of the newly discovered hydrothermal fields located on the spreading segments 27–28 between the Indomed and Gallieni transform faults (Figure S1 in the supporting information). Geophysical surveys of this region [*Georgen et al*., 2001; *Sauter et al*., 2001, 2004; *Tao et al*., 2009] have revealed that this part of the SWIR has experienced a dramatic increase in magma supply since 8–10 Ma. This active hydrothermal field is characterized by a distinct anomalous temperature (up to 2.5°C) and turbidity in the water column and located at 49°39′E, 37°47′S on the segment 28. Photographs taken by the autonomous underwater vehicle Autonomous Benthic Explorer revealed black smoke rising from the seafloor in the location of the temperature anomalies [*Tao et al*., 2012]. Metal sulfides and relict chimneys and yellow to brown low-temperature deposits are pervasive in this area along with abundant molluscs and gastropod shells. In this study, we have examined the Fe- and Si-rich hydrothermal sediment samples obtained in this hydrothermal field aiming to investigate their formation and the controlling factors, especially the critical role that the microbe has played in this process.

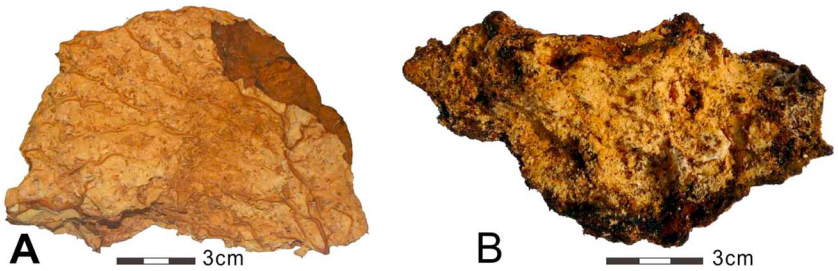

Figure 1. Typical low-temperature Fe-Si oxyhydroxide samples used in current study on the SWIR. (a) Yellow Fe-Si oxyhydroxide, note the brown to ocherous veins, sample SH5. (b) Yellow Fe-Si oxyhydroxide crust with black Mn oxide impregnated, sample SH7. The scar bars are shown below the sample in both subfigures.

3. Materials and Methods

The research carried out here was based on samples collected from the newly discovered hydrothermal fields along the SWIR during the DY115-20 expedition of R/V *DaYang YiHao* from October 2008 to March 2009. By using TV-guided grab, we have collected four samples, labeled as SH5, SH7, SH8, and SL9, respectively, to use in this study. Some samples were loose and yellowish with vague vein (brown to ochreous; width, 0.5–1 cm) structure occurring in them (Figure 1a). Semiconsolidated crusts were occasionally observed covering yellow parts of these deposits, inside which filamentous soft materials occurred with a brighter yellow coloration (Figure 1b). After macroscopic description of the samples, they were taken on deck, frozen, and stored at −20°C.

For detailed petrographic investigation, the hydrothermal samples were dehydrated under vacuum, impregnated with epoxy resin, and sectioned for petrographic analysis. Dehydration was achieved by freeze drying. The dried samples were then impregnated with a polyester resin mixed under vacuum, and eight polished thin sections were prepared following the method of *Camuti and McGuire* [1999]. The thin sections were examined using transmitted light microscopy.

The mineralogical characterization of the samples included X-ray diffraction and infrared spectroscopy using powdered samples. Morphological and microtextural observations were made using a field emission scanning electron microscope equipped with an energy-dispersive spectrometer for microanalysis, using a Hitachi S4800 instrument (operating conditions 3.0 kV with a range of variation of 7.5–13.6 mm) at the China University of Petroleum in Qingdao.

X-ray diffraction analysis of pressed powder samples was carried out using an automatic PANalytical X'Pert system. Diffraction patterns in the 2.5–80° 2θ range were obtained using a 0.02° 2θ step scan and 50 s counting time. Operating conditions were 40 kV and 28 mA, using CuKα radiation (1.54061 Å) and a graphite monochromator.

Small fragments of sample SH7 fixed in 4% gluteraldehyde were prepared for transmission electron microscopy by washing 3 times in a 0.1 M phosphate buffer at pH 7.4, further fixed with osmium tetroxide at 4°C for 2 h, and dehydrated through a series of ethanol solutions. The dehydrated samples were then washed twice in propylene oxide, followed by an overnight stand in a 50/50 mixture of propylene oxide and Agar100 resin, and then transferred into fresh embedding tubes and polymerized at 60°C for a further 24 h. They were then sectioned on an ultramicrotome, mounted on copper grids, stained with uranyl acetate, and lead citrate to improve the contrast under investigations. Transmission electron microscopy analysis was performed using an FEI Tecnai 12 transmission electron microscope and a JEM-2010HR transmission electron microscope operating at 100 kV. Energy-dispersive X-ray spectroscopy was conducted at 100 kV on an Oxford INCA Energy transmission electron microscope X-ray energy-dispersive spectrometer. Mineral structure was determined by transmission electron microscopy using selected area electron diffraction.

The spatial distribution of the major and trace elements in different samples was determined using electron microprobe analysis (EMPA, JEOL JXA-8100) operating at conditions of 20 kV acceleration voltage, 50 nA current beam with a 1–2 μm beam width. Prior to analysis, a 10–20 nm thick carbon layer was splutter coated on the polished sections. Calibration data for the various elements, including spectral lines and analyzing crystals for each element, are given in Table S1 in the supporting information.

Fourier transform infrared spectroscopy was used at room temperature using a Nicolet 380 Fourier transform infrared (FTIR) spectrometer. The Fourier transform infrared spectroscopy spectra were recorded in the 4000 to 400 cm^{-1} range and were collected after 256 scans at 4 cm^{-1} resolution. The KBr disk technique was used for sample preparation. The KBr (FTIR grade, Fluka) was dried at 200°C for 24 h. To prepare the KBr pellets, 1 mg of RM sample (derived from the RM-As(V) samples at pH 4, 7, and 10 at the last point of isotherms and after the extraction of RM-As(V) samples at pH 4) was grounded for 1–2 min together with 200 mg of KBr. The pellets were made using 90 mg of the KBr-RM mixture. This mixture was then pressed in a dye under vacuum for 4–6 min at 12 t pressure to produce transparent disks about 1 mm thick and 13 mm in diameter. An empty KBr pellet was used as reference, and its spectrum was subtracted from the sample spectrum to suppress spectral artifacts caused by KBr impurities and water.

X-ray computed tomography is a nondestructive technique for visualizing interior features within solid objects, which has been used to obtain digital information on the three-dimensional geometry and property information of the Fe-Si oxyhydroxide deposits. The apparatus used is a high-resolution industrial microcomputed tomography (CT) (type: GE sensing and inspection technologies GmbH Phoenix X-ray, minimum resolution: 500 nm). The X-ray parameters are adjusted to 100 kV (voltage) and 50 μA (current) so that the sample could be penetrated and a clear CT image could be obtained by the flat detector. During the measurement, the sample was loaded on the autorotation stage and rotated 360° for a whole CT scanning. The magnification is 81.54, which results in a voxel size (i.e., resolution) of 2.45 μm.

4. Results

4.1. X-ray Diffraction Analysis

X-ray diffraction analysis showed that poorly crystalline ferrihydrite and amorphous opal are common in these samples (Figures S2a and S2b in the supporting information). The ferrihydrite is characterized by two main broad peaks at $d = 2.6$ Å and $d = 1.5$ Å (Figure S2a in the supporting information). But their X-ray diffraction patterns were different from those of typical two-line ferrihydrite in the relative intensities of the two peaks [*Parfitt et al*., 1992; *Zhao et al*., 1994; *Rancourt et al*., 2001]. In typical two-line ferrihydrite, the first peak at 2.6 Å is generally more intense than the peak at 1.5 Å. Our results hint at appreciable Fe-O-Si linkages on the ferrihydrite surface [*Kukkadapu et al*., 2004]. The X-ray diffraction pattern of opal contains a single broad peak at $d = 4.0$–4.1 Å (Figure S2b in the supporting information), which is similar to those previously identified from the Juan de Fuca Ridge [*Toner et al*., 2009] and Lohi Seamount [*Toner et al*., 2012]. By contrast, more crystalline birnessite and minor nontronite have been identified in these samples (Figure S2c in the supporting information). Most often, birnessite and minor nontronite occur with significant amounts of opal, indicating that opal is widespread in these low-temperature deposits. Also, in some samples, abundant nontronite and birnessite occur without opal and ferrihydrite (Figure S2d in the supporting information).

4.2. Optical Microscopy

As shown in Figure 2, most of the filaments have lengths of between 10 and 100 μm and diameters of between 2 and 10 μm and display complex intertwining and twisting of the filaments which occurs in the form of chains of beads (Figure 2a), very similar to the observation of *Little et al.* [2004]. The blebs on the surface of the filament typically have diameters of between 1.0 and 1.5 μm (Figure 2a), possibly indicating that the blebs were precipitated separately by surface adsorption after the filament formation. Altogether, three main structures were observed in the filamentous mats: (1) a mesh-like structure weaved by several single filaments in which no material occupies the mesh as shown in Figures 2a and 2b; (2) radiating structures which are, in general, located in the dense substrate of the Fe oxides as shown in Figure 2c; and (3) bundles of rod-like structures. All the rod-like structures have roughly the same direction, diameter, and length as shown in Figure 2d. These aforementioned observations have also occurred in the other hydrothermal vents [e.g., *Little et al*., 2004; *Sun et al*., 2013].

4.3. Field Emission Scanning Electron Microscope Analysis

As shown in Figure 3, various structures were observed by field emission scanning electron microscope. The tortuous filaments are characterized by their smooth surfaces and are always associated with small spheres which have diameters of about 1–3 μm (Figure 3a). Rod-like structures also occur in some samples (Figure 3b). By contrast with the observations made by optical microscopy, the rod-like structures often

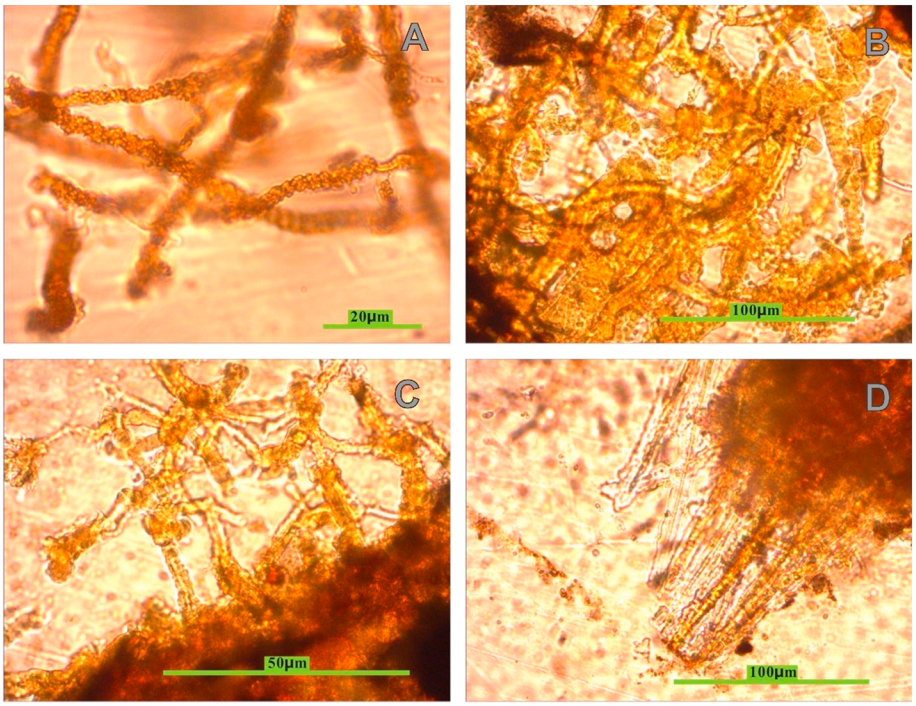

Figure 2. Photomicrographs of Fe-Si oxyhydroxide from the SWIR in plane-polarized light (thin sections). (a) Morphology of individual filament, note the precipitation of tiny Fe-containing spheres on the surface, sample SH5. (b) Filaments crossing with each other to form a mesh structure, sample SH7. (c) Radiating structures located in the dense substrate of the Fe oxides, sample SH7. (d) Bundles of rod-like structures with dense flocculent precipitation, sample SL9.

display smooth surfaces (Figure 3b). Further, twisted structures were also found in our samples (Figure 3c), which could be reasonably assumed to be produced by FeOB, *Mariprofundus ferrooxydans*, described in previous studies [e.g., *Emerson et al*., 2007; *Edwards et al*., 2011; *Fleming et al*., 2013]. Sometimes, the twisted structures are surrounded by amorphous silica precipitates (Figure 3d). These samples are composed of O, Fe, Si, P, and minor Na and Cl based on energy-dispersive spectrometer analyses (Figures 3e and 3f), with a molar Si: Fe ratio in the range of 0.67–0.72 (data not shown). It is noteworthy that filaments with more exquisite details representing the biogenic structure contain significantly higher content of Fe than those with more vague outlines.

In addition, amorphous Si-rich structures were detected using scanning electronic microscopy and energy-dispersive spectrometer. Silica generally occurs as numerous spheres encased on the surface of preformed filaments, leading to the obvious accretion in diameters (Figure S3 in the supporting information). The diameter of the silica sphere, which ranges from 100 to 200 nm, is typically less than the diameter of the biogenically produced Fe-oxide structure. The second Si-rich structure occurs as aggregation of the spheres attached to flat substrates, and the individual spheres also have homogenous diameters (Figure S3b in the supporting information). Another special structure was observed in our sample containing Fe-rich oxyhydroxide filament in the center and amorphous silica in the outer (Figure S3d in the supporting information). All the distribution patterns of the silica sphere described above display a characteristic "two-generation" model in these low-temperature Fe-Si oxyhydroxide deposits. On the basis of energy-dispersive spectrometer analysis, the main components of the spheres are Si, O, and minor Fe (Figure S3c in the supporting information), with the X-ray diffraction determinations demonstrating that the Si-rich oxide is opal A.

4.4. Transmission Electron Microscopy and Selected Area Electron Diffraction

Mineralized bacteria investigated by transmission electron microscopy show a ring structure of the cell walls (Figure 4a). These cell walls are formed from a series of fine tiny needle-like filaments which consist mainly of Fe, Si, O, Mg, and C based on the energy-dispersive spectrometer analysis (Figure 4b). A single

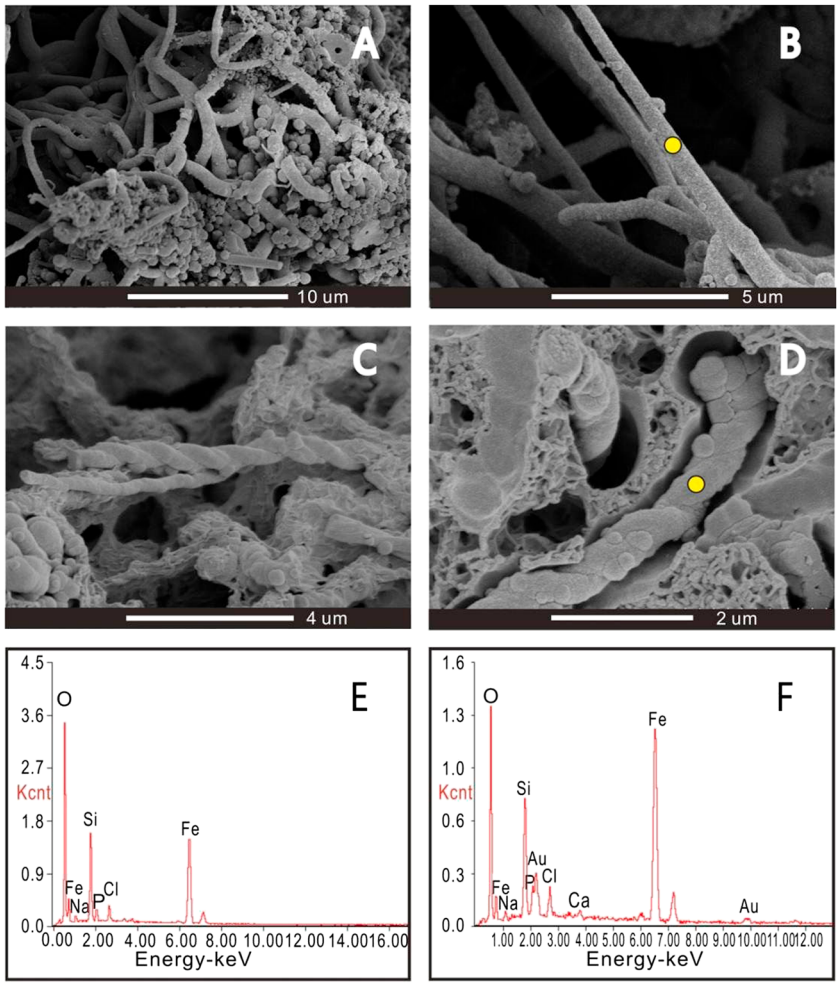

Figure 3. Scanning electronic microscopy photographs and energy-dispersive spectrometer spectra of hydrothermal Fe-Si oxyhydroxides from the SWIR. (a) Filamentous structure of Fe-Si oxyhydroxide with clusters of small spheres. (b) Straight sheaths, sample SL9; the yellow dot indicates the position of energy-dispersive spectrometer. (c) *Mariprofundus ferrooxydans*-like twisted stalk sample. (d) *Mariprofundus ferrooxydans*-like twisted stalks surrounded by silica precipitates indicating that the Fe-rich filament formed before the silica, sample SL9; the yellow dot indicates the position of energy-dispersive spectrometer. (e) Energy-dispersive spectrometer spectrum of the straight sheaths shown in Figure 3b. (f) Energy-dispersive spectrometer spectrum of the twisted stalk shown in Figure 3d.

mineralized cell was observed in the samples which underwent intracellular mineralization, and the remnant cytoplasmic material was replaced with amorphous iron-silica hydroxide (Figures 4c and 4d). Some tortuous longer filaments were also present in the vicinity of the mineralized cell (as the arrow shows), indicating the presence of extracellular materials. The selected area electron diffraction pattern of the amorphous iron hydroxide forming the mineralized cell exhibits two broad rings corresponding to distances of 0.15 and 0.26 nm (Figure 4e). A similar selected area electron diffraction pattern was measured from a reference two-line ferrihydrite. The transmission electron microscopy and selected area electron diffraction data are strong indications that the mineralized Fe-rich oxide observed here is two-line ferrihydrite [*Gloter et al*., 2004]. Moreover, energy-dispersive spectrometer analysis showed that Si, Fe, C, and O were the major elements of the mineralized intracellular cytoplasmic material (Figure 4f).

4.5. Electron Microprobe Analysis

A single filament was examined based on the elemental mapping analysis in one polished section of the low-temperature hydrothermal deposit (Figure 5). At a micron level, the filament that is embedded in Mn oxide shows a marked enrichment of Si and Fe. In the center of the filament, it shows a close affinity

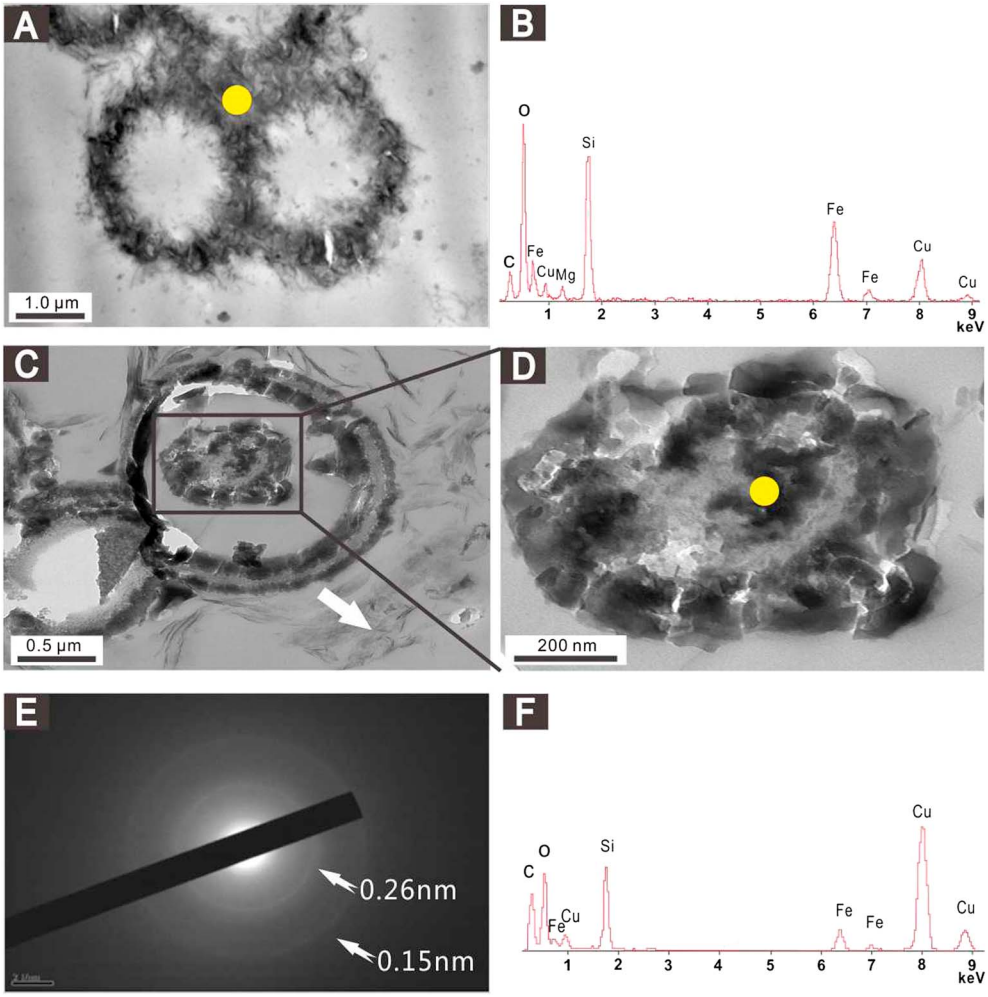

Figure 4. Transmission electron microscopy micrographs of low-temperature hydrothermal Fe-Si oxyhydroxide sample from the SWIR. (a) The ring structure of the mineralized cell walls, sample SH5; the yellow dot indicates the position of energy-dispersive spectrometer. (b) Energy-dispersive spectrometer spectrum of the ring structure presented in Figure 4a showing that the main peaks are Si, Fe, C, and O. Element Cu is from Cu grid. (c) A fully mineralized cell consisting of fine needle-like filaments and extracellular polymeric substances (as indicated by the arrow), sample SH8. (d) The enlargement of pane in Figure 4c showed the mineralized cytoplasmic material; the yellow dot indicates the position of energy-dispersive spectrometer. (e) Selected area electron diffraction pattern of the mineralized cell in Figure 4b showing a characteristic two-line ferrihydrite with two broad rings corresponding to distances of 0.15 and 0.26 nm, respectively. (f) Energy-dispersive spectrometer spectrum of the mineralized intracellular material presented in Figure 4d showing that the main peaks are Si, Fe, C, and O. Element Cu is from Cu grid.

between Fe and Mn distributions despite, whereas in the center and edge of the filament, Fe appears to be more enriched, indicating that the incorporation of later silica is not completed.

On a larger scale (tens of microns), distinctive layer structures have been observed in these deposits. The layers almost composed of Fe along with minor Mn are nearly isopachous with a width ranging from 50 to 80 μm (Figure 6). The boundary between the ferruginous and siliceous layers is obviously abrupt in most samples, whereas some Fe-rich layers contain vague interfaces between Si-rich layers with some Fe-rich cores embedded in the Si-rich layers (Figure 6). However, some samples show no obvious layer structure during examination (Figure S4 in the supporting information). Even in the latter case, much of the Fe-rich core and filaments are also observed to exist in the Si-rich layers. These separate filaments along with irregular Fe-rich cores in Si-rich parts are reminiscent of the radiating structures located in the dense substrate of the Fe oxides during the microscopic investigation. Overall, Fe and Si have an enantiomorphous distribution

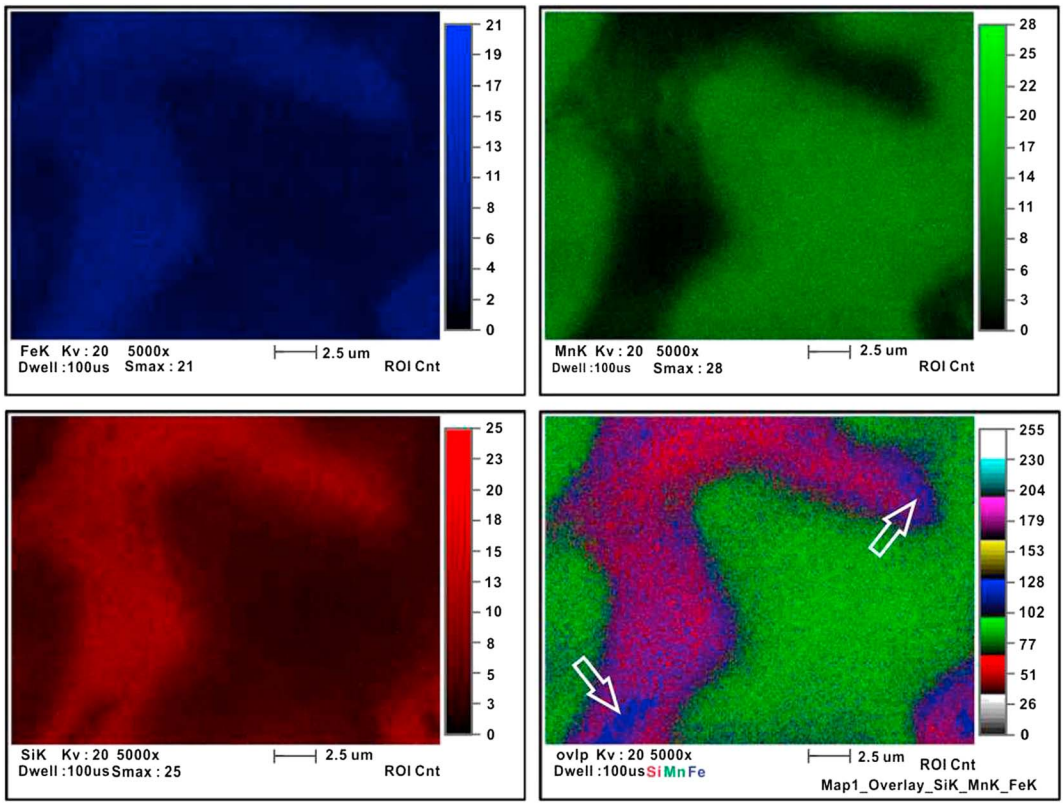

Figure 5. Elemental mapping of an individual filament from Fe-Si oxyhydroxide deposits, which shows that the filament are enriched in Fe and Si and embed in the Mn oxide matrix. Also note that Fe is more intense in the center and wedge of the filament (as pointed by the hollow white arrows), indicating that the incorporation of later silica is not completed. Sample SH7.

according to the mapping data. With regard to Mn, there is always an obvious relationship between Fe, although in most samples, Mn is completely absent. Further, the distribution of P appears to have a relationship with Fe oxyhydroxide in some samples (Figure 6), whereas Zn is nearly absent in all examined samples (Figure 6 and Figure S4 in the supporting information).

4.6. Fourier Transform Infrared Spectroscopy Analysis

Three samples (SH7, SH8, and SL9) investigated here display similar Fourier transform infrared spectroscopy spectral features (Table 1 and Figure 7). Infrared absorption spectra (Figure 7) show two distinct bands at 3352–3396 cm^{-1} and approximately 1620 cm^{-1}, which indicate the presence of molecular water [*Koji and Solomon*, 1977]. The asymmetric Si-O stretching vibrations at the peak of 1007–1090 cm^{-1} are derived from the vibrations of SiO_4 tetrahedra with three or four bridging oxygen atoms [*Lazarev*, 1972; *Farmer*, 1974]. The obvious shift of the peak from about 1000 cm^{-1} (1007 cm^{-1} for SH7) to higher wave numbers (1057 cm^{-1} for SL8 and 1090 cm^{-1} for SH8) may reflect the presence of unpolymerized or poorly polymerized silica up to the fully polymerized silica [*Carlson and Schwertmann*, 1981]. A medium intensity band at 945–947 cm^{-1} can be assigned to Si-O-Fe stretching [*Carlson and Schwertmann*, 1981]. The 789–793 cm^{-1} band is assigned to the Si-O stretching vibrations of the SiO_4 ring structure. This is usually correlated with fully condensed Si atoms surrounded by four Si-O-Si linkages [*Landmesser et al.*, 1997]. The band at about 461–496 cm^{-1} can be regarded as resulting from the stretching vibration of Fe-O [*Vempati and Loeppert*, 1989; *Ying et al.*, 2007] suggesting the presence of ferrihydrite [*Vempati et al.*, 1990]. The small band near 3675 cm^{-1} is generally assigned to the O-H stretching vibrations of the OH group attached to P [*Suzuki et al.*, 2011].

4.7. X-ray Computed Tomography

The X-ray computed tomography (X-CT) image is shown in Figure 8. Because the computed tomography image mainly reflects a density difference of the inner sample, it is obviously observed that there are two

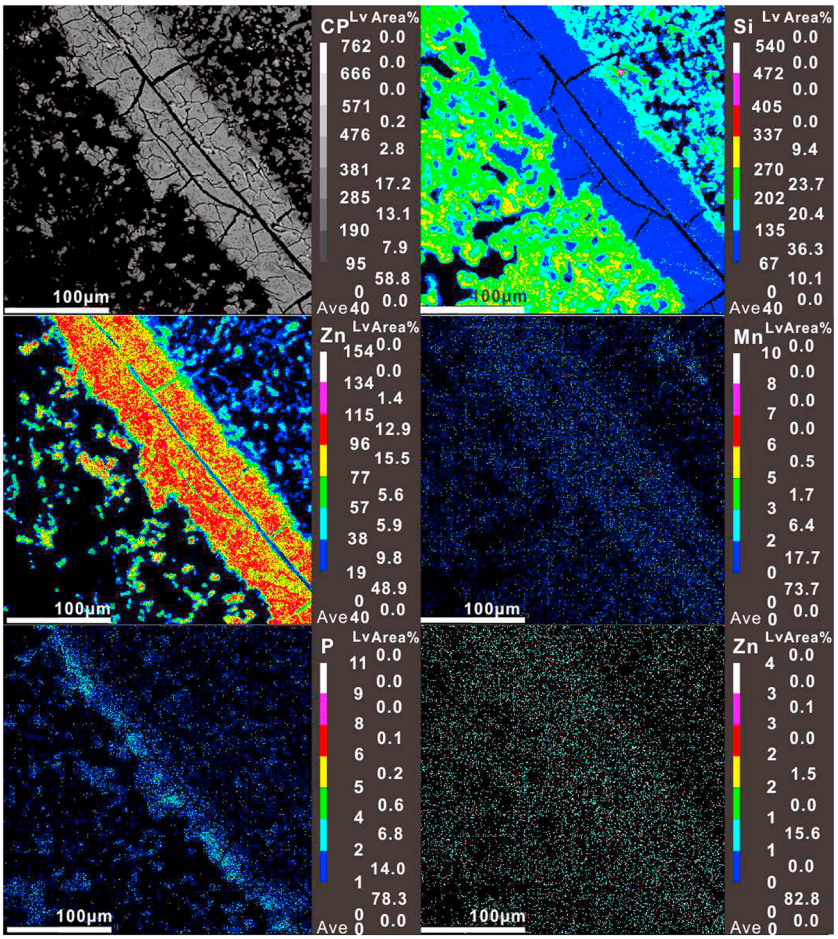

Figure 6. EMPA elemental mapping of Si, Fe, Mn, P, and Zn in the low-temperature hydrothermal deposit, sample SH7. The colorful concentration bars of every element are presented in the right. The grayish white layer in CP (backscattered electron image) is enriched in Fe along with minor P, showing an affinity between Fe oxide and P. There is an abrupt edge between Si-rich layer and Fe-rich layer; some debris-like Fe-rich matters, however, exist in the Si-rich layer; manganese and Zn show no close affinity with Si or Fe oxides. Also note that the maximum length of the fractures is 3.5 μm following dehydration during the preparation of the thin sections.

Table 1. Frequencies and Band Assignments for the Characteristic Vibrations Found in the FTIR Absorption Spectra of Fe-Si Oxyhydroxide Precipitates of the SWIR[a]

Bands	Wave Numbers (cm^{-1})	Assignments[b]
1	461–496	ν_{as} Fe-O-Si
2	536–540	ν_s Fe-OH
3	789–793	ν_s Si-O-Si
4	945–947	ν Fe-O-Si
5	1007–1090	ν_s Si-O/Si-OH
6	1620–1628	δ H-O-H
7	3352–3396	ν Si-OH
8	3675	ν P-O-H

[a]In this structure, silica substitutes for double-corner FeO_6-octahedra in Fe oxyhydroxide polymeric complexes existing at the early stages of Fe(III) hydrolysis [*Pokrovski et al.*, 2003].
[b]Parameters ν = stretching, δ = bending, *as* = asymmetric, and *s* = symmetric.

high-density layers in the sample. According to the electron microprobe analysis examination, these high-density mineral phase belts are Fe-rich layer structures with a width in the range of 50–100 μm, while the relative low-density mineral phase are silica-rich layer. The sample used in the X-ray computed tomography examination was randomly cut from a bigger natural sample (SH7); it therefore shows that Fe-rich layers occur widely in this sample. Furthermore, the high-density layer structure has

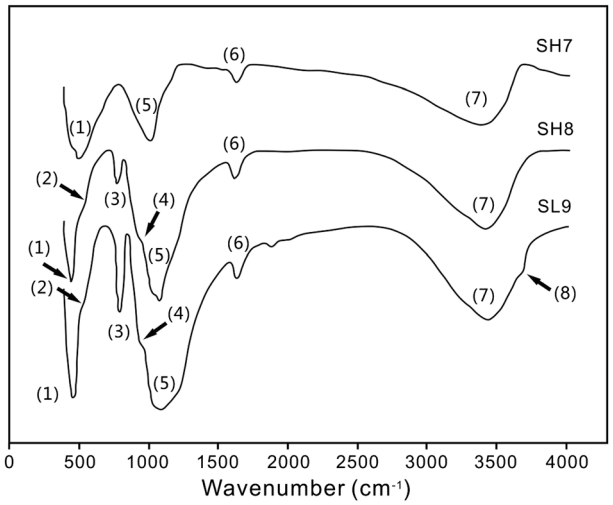

Figure 7. Fourier transform infrared spectra of hydrothermal Fe-Si oxyhydroxides from the SWIR. The numbers in brackets mark the peak positions of the wave numbers corresponding to the band numbers in Table 1. Samples SH7, SH8, and SL9.

also been detected on a larger scale during X-CT analysis, indicating that it is common in these hydrothermal sediments.

5. Discussion

5.1. Iron Mineralization in Low-Temperature Hydrothermal Environment

Increasing evidences suggested that neutrophilic FeOB played a significant role in the formation of Fe-Si oxyhydroxide at modern seafloor low-temperature hydrothermal fields [e.g., *Kennedy et al*., 2003a, 2003b, 2004; *Little et al*., 2004; *Emerson and Moyer*, 2002; *Edwards et al*., 2011; *Li et al*., 2013; *Sun et al*., 2013]. In our study, various microfossils described by scanning electronic microscopy examinations indicated their presence

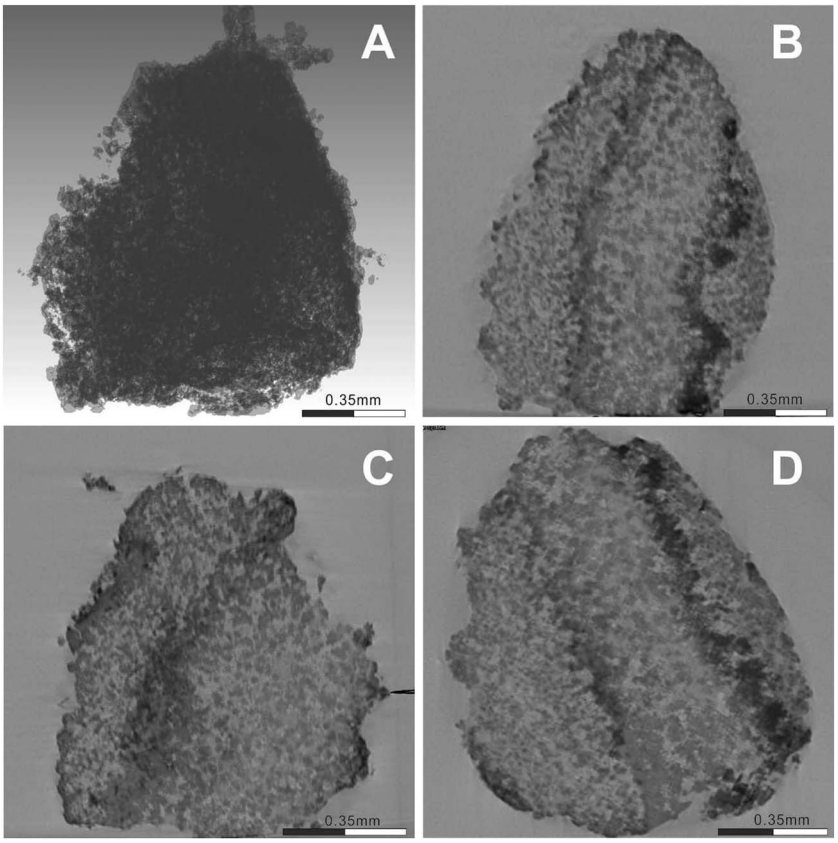

Figure 8. Three-dimensional reconstruction of the X-ray CT imagery at a spatial resolution of 2.45 μm. Images obtained by direct X-ray CT scan come from four directions, they are (a) front, (b) left, (c) top, and (d) right, respectively. Sample SH7. Note that the two belts with dark color distribute spatially in the sample.

in the low-temperature hydrothermal environments at SWIR. Obvious twisted filaments are indicative of *Mariprofundus ferrooxydans*, while tubular sheath-like filaments bear a strong resemblance to an unculutured sheath-forming *Zetaproteobacteria* [e.g., *Fleming et al*., 2013]. Simultaneously, our parallel molecular biological study [*Li et al*., 2013] based on the same samples has revealed that neutrophilic FeOB, including *Mariprofundus ferrooxydans* and some other species of *Zetaproteobacteria*, indeed account for a major proportion of the bacterial communities of these hydrothermal Fe-Si oxyhydroxide deposits.

It is well known that Fe-oxidation attributed to cellular activity and autocatalysis (occurring on iron oxide surfaces and bacterial surfaces) is an important process and probably accounts for a significant proportion of the total iron oxidation that occurs in the natural systems. With respect to the cellular activity, it involves a process that the FeOB, such as *Mariprofundus ferrooxydans*, use Fe^{2+} as an energy source by oxidizing it to Fe^{3+} in the bacterial cells, most likely in the cell envelope, including the plasma membrane [*Suzuki et al*., 2011]. In this biologic process, they prefer to localize the mineralization outside the cells in order to avoid encrustation. Thus, the initial extracellular stalk- or sheath-like structures composed primarily of Fe oxyhydroxides were produced during its growth [*Emerson et al*., 2007].

On the other hand, some clues also indicated that the autocatalysis of Fe oxidation cannot be excluded in this study. Specifically, an interesting feature is the unusual size of the mineralized sheaths and stalks in these deposits. As evidenced by optical microscope examinations (Figure 2), the various filaments (width, 2–10 μm) are much wider than that the normal sheaths and twisted stalks of FeOB (width, 0.5–3 μm [*Suzuki et al*., 2011]). With respect to this phenomenon, the most plausible explanation is that after being abandoned by active Fe-oxidizing bacteria, gelatinous Fe oxide continues to precipitate on the surface of the filaments. This is due to the byproducts of Fe-oxidation, Fe(III) hydroxide, that can further accelerate oxygenation of Fe^{2+} ions by homogeneous or heterogeneous reaction in the neutral aquatic environments [*Tamura et al*., 1976]. In such a case, the surface of mineralized sheaths and stalks can simply act as available nucleation sites. As a result, we now observe the accretion of the filaments in diameter as well as the bleb-like structures in their surface.

As mentioned above, the results of this study further suggest that FeOB harnessing Fe^{2+} as an energy source would compete with their own byproducts for growth in the hydrothermal environments. However, it is difficult to estimate the exact percentage of ferric oxide formed merely by inorganic binding process or by enzymatic oxidation based solely on our study. *Rentz et al.* [2007] reported that the rates of Fe oxidation for cellular processes and autocatalysis were in the same order of magnitude based on a series of simulation experiments. Being comparable to their results, *Emerson and Moyer* [2002] have pointed out that up to 60% of the iron oxide deposition (the combination of sheaths and filaments) at a number of the Loihi vents located around 35 km off the southeast coast of the island of Hawaii is directly attributable to microbial activity. This may represent a good constraint of this question.

5.2. Si Precipitation in the Low-Temperature Hydrothermal Environments

The role of microbes in the formation of Si-rich mineralized structures has been addressed by a number of previous studies [e.g., *Yee et al*., 2003; *Jones et al*., 2004; *Peng et al*., 2011; *Li et al*., 2013]. Nearly all of them suggested that its formation was controlled primarily by abiogenic processes such as silica supersaturation and subsequent polymerization [*Konhauser et al*., 2004; *Jones et al*., 2004]. In this passive process, the cell surfaces merely act as SiO_2 templates [*Fein et al*., 2002; *Guidry and Chafetz*, 2002; *Yee et al*., 2003; *Rodgers et al*., 2004; *Tobler et al*., 2008]. From the result of the current study, we totally agree this conclusion. Besides this, the observation that two-generation structure, Fe-rich core of filaments embedded in the Si-rich parts, and existence of the Fe-O-Si and Si-O-Si bonds, all suggest that the mechanism involved in silica precipitation is representing a later generation with two-step process. This finding was also consistent with the previous finding [*Beveridge and Fyfe*, 1985; *Sun et al*., 2012].

We propose that the Fe-O-Si bond (at 945–947 cm^{-1}) was a consequence of the surface binding of Si to Fe-OH functional groups of Fe oxide. Whereas, the Si-O-Si bond (789–793 cm^{-1}) represents polymerization when the Si:Fe molar ratio of the hydrothermal fluids increases to a value greater than 0.2 [*Swedlund and Webster*, 1999]. As a result, monomeric silica can bind directly onto ferrihydrite surface sites and substitute for double-cornered FeO_6 octahedra in Fe-oxyhydroxide polymeric complexes [*Pokrovski et al*., 2003] at low-Si concentrations (characterized by undersaturation). Meanwhile, when the dissolved Si reaches saturation, the ferrihydrite surfaces can act as a template for silica polymerization.

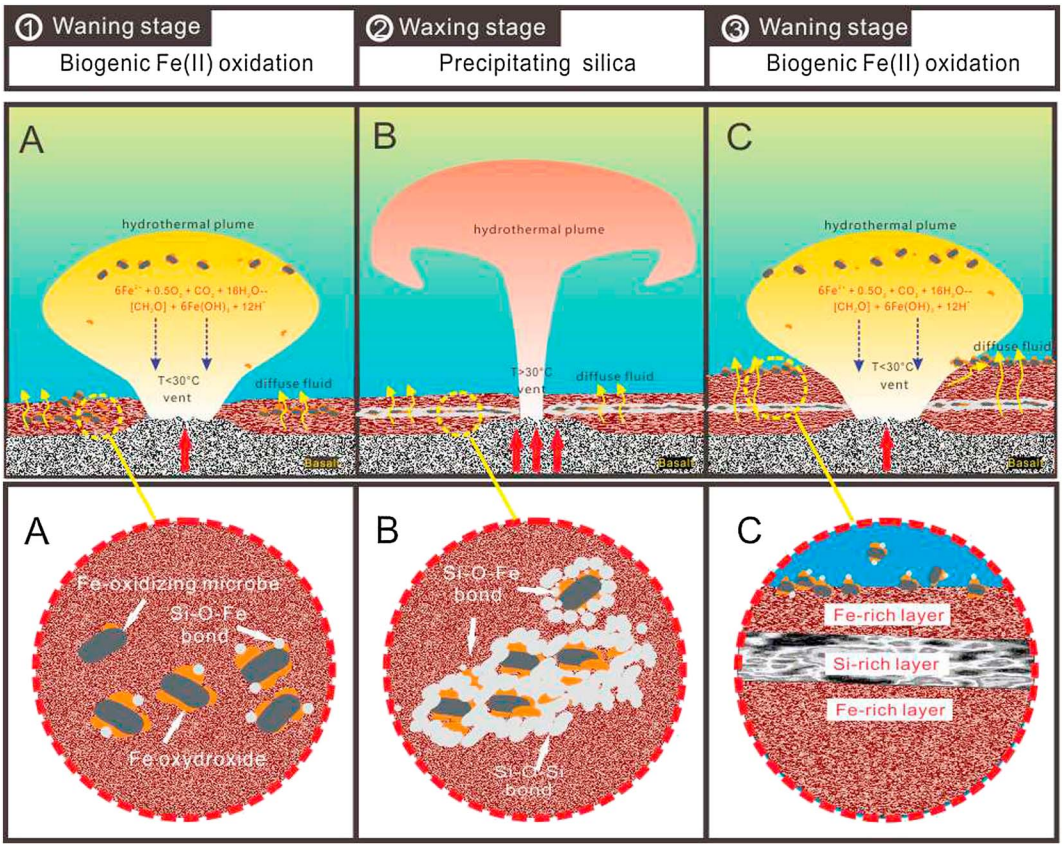

Figure 9. Scenario of episodic recharge and precipitation events by pulses of hydrothermal fluids and the formation of alternating Fe- and Si-rich layers. In a waning stage of hydrothermal activity, chemolithoautotrophic Fe-oxidizing microbe living in an optimal range can oxidize hydrothermal reducing Fe(II) to $Fe(OH)_3$ in order to obtain energy to sustain their growth (see carton from A); in this stage, Fe-rich microlayer occurs. In a waxing stage of hydrothermal activity, the suitable niche of chemolithoautotrophic Fe-oxidizing microbe has been destroyed. Fe oxyhydroxide formation decreases, whereas abundant silica precipitates from a pristine fluid near the venting site by means of binding to preformed Fe oxyhydroxide surface or polymerization (see carton from B); in this stage, Si-rich layer dominates the deposits. Thus, the alternating Fe- and Si-rich layer structure forms in the vicinity of modern seafloor hydrothermal vents.

An important question then is how the dissolved Si in the hydrothermal fluids reaches the saturation state. In fact, the view that conductive cooling mechanism leads to precipitation of silica in modern hydrothermal vent system is currently in favor with most workers [*Juniper and Fouquet*, 1988; *Peng et al.*, 2011; *Sun et al.*, 2012]. The solution then becomes supersaturated with respect to amorphous silica as a result of the conductive cooling, and subsequently, it initiates spontaneous Si polymerization. Thus, Si-rich layers in low-temperature hydrothermal deposits are formed.

5.3. An Ideal Genetic Model for the Alternating Fe- and Si-Rich Bandings

Another important observation of this study is the Fe-rich microlayer alternating with the Si-rich microlayer within the SWIR hydrothermal deposits. For some samples, there are even some abrupt edges existing between the two layers. Furthermore, the Fe-rich layers are nearly isopachous and run parallel to each other (see Figures 6 and 9). To our knowledge, a formation mechanism of this alternating model in the modern marine hydrothermal environments has not been deeply discussed before.

Generally, we can speculate that the Fe-rich microlayer represents an ideal niche (such as temperature and reduced Fe supply) for FeOB, whereas Si-rich microlayer represents an abiotic optimum condition from which silica could precipitate easily. As mentioned above, no matter the abiotic and biotic process, FeOB actually played a significant role in the formation of Fe-rich microlayer, while mineralized structures composed of silica is controlled primarily by abiogenic processes. Therefore, the relative ratios between iron

and silica oxides in these deposits may reflect the activity of Fe-oxidizing microbes to some extent in this low-temperature hydrothermal environment. Meanwhile, the activity of Fe-oxidizing microbes was closely related to the environmental temperature, which was mainly influenced by the hydrothermal process. Thus, we tentatively consider the temperature of hydrothermal fluids to be a critical factor which controls the deposition of Fe and Si oxides.

As revealed in previous study [*Emerson et al*., 2007], the optimum growth temperatures of the representative FeOB *Mariprofundus ferrooxydans* are 10–30°C. When the temperature of the hydrothermal habitant was favorable for the Fe-oxidizing microbes, more Fe oxide would be precipitated and Fe-rich banding form. Inversely, when the temperatures were unfavorable, Si-rich banding would form. Namely, below or above this fluid temperature range, biogenic iron precipitation would decrease, and the precipitation of iron and silica oxides would be decoupled [*Posth et al*., 2008]. However, rather than $<$10°C, we prefer the scenario that massive silica precipitation was in temperature above 30°C, since normal modern seawater is poor in dissolved Si^{4+}. This conclusion is also consistent with the precipitation temperature range (38.3–81.8°C) of silica deduced from oxygen isotopic compositions of amorphous silica by our previous study [*Li et al*., 2013]. It means that a large-scale silica precipitation may occur in a waxing stage of the hydrothermal activity. Therefore, we think that the fluctuations of the hydrothermal activity was the main factors which led to the primary layering by successive cycles of microbial catalyzed iron(III) mineral deposition and abiotic silica precipitation. The waxing and waning discharge in modern seafloor hydrothermal system may be triggered by episodic hydrothermal activity, which is ultimately controlled by the episodic magmatic intrusion events at the ridge axis [*Baker et al*., 1995; *Massoth et al*., 1994, 1998]. For instance, the episodic venting of hydrothermal fluids (megaplume) has been observed at least 3 times as a rapid field response to the seismic activity on the Juan de Fuca Ridge between 3 and 26 July 1993 [*Baker et al*., 1995].This presumed scenario of episodic waning and waxing hydrothermal activities and the genetic model of alternating Fe and Si layers are presented in Figure 9.

5.4. Implications for the Formation of Ancient BIFs

Despite a century of intensive endeavor, the deposition of ancient iron formations especially BIFs in ferruginous oceans still remains an enigma, although seafloor hydrothermal fluids are now well accepted to provide iron source for these formations [e.g., *Holland*, 1973; *Simonson*, 1985; *Dymek and Klein*, 1988]. Two important cruxes of the BIF enigma are (i) by what means the huge amounts of ferrous iron get oxidized prior to the onset of oxygenated conditions and (ii) how the spectacular alternating BIF banding formed. Our current study happens to implicate both questions. One meaningful finding of this study is that microaerobic chemolithoautotrophic FeOB would be responsible for the oxidation of ferrous iron in the hydrothermal environment. The rare earth element and iron isotope analysis in previous study has showed that low-oxygen condition, providing a propitious setting for the proliferation of chemolithotrophic iron-oxidizing bacteria, is presented in the late Paleoproterozoic redox-stratified oceans [e.g., *Holm*, 1987b; *Emerson and Moyer*, 1997; *Planavsky et al*., 2009]. Simultaneously, the microfossil evidences from the Animikie Basin iron formations (late Paleoproterozoic) indeed found the clues of a predominance of microaerophilic iron oxidizers [*Planavsky et al*., 2009], which were comparable to the present-day *Lepothrix*, *Gallionella*, and *Mariprofundus* [*Barghoorn and Tyler*, 1965; *Strother and Tobin*, 1987; *Golubic and Lee*, 1999]. Moreover, the fossilized iron bacteria in our samples have been recognized as microaerobic FeOB by using molecular biological methods, revealing that chemolithoautotrophic microbe might be an appealing option to oxidize the ferrous iron in the ancient oceans in addition to the generally accepted anoxygenic phototrophic bacteria [*Cloud*, 1973; *Widdel et al*., 1993; *Kappler et al*., 2005; *Posth et al*., 2008; *Fru et al*., 2013]. This suggestion undoubtedly pushes the formation environment of ancient iron formation to much wider deep sea rather than long-speculated shallow area of ancient oceans.

With regards to the second crux, the distinctive alternated laminae between Fe-rich layer and Si-rich layer, occurring in the hydrothermal deposits on the SWIR, are also reminiscent of a quintessential feature of BIFs. We have already discussed that if the environment is optimum for FeOB to habit, the precipitation of Si is relatively restricted except for only minor silica incorporated owing to physiochemical sorption. This may hint at rigid precipitation conditions that determine which type of precipitation can occur. For this regard, the alternating Fe- and Si-rich layers in our samples are actually products of episodic pulse of hydrothermal fluid contributions. However, as the seawater in the Precambrian Ocean is known to be saturated relative to amorphous silica due to the absence of silica-secreting organisms [*Siever*, 1992; *Treguer et al*., 1995],

conductive cooling would not be the key factor that gives rise to the silica precipitation on a larger scale. For instance, *Eugster and Ming-Chou* [1973] suggested that evaporation was the reason, while *Posth et al.* [2008] argued that temperature fluctuations of seawater could be the driving force. These potential reasons provide a more reasonable explanation for the occurrence of more extensive horizontally continuous mesobands (millimeters to decimeters, such as in Hamersley Group Iron Formations [*Morris*, 1993]) and even thinner microband (~3–12 μm [*Li*, 2014]). No matter which factor exerts a role in this process, our finding has demonstrated that alternated laminae structure comparable to ancient BIFs indeed could form in seafloor hydrothermal systems.

Given the significant differences of spatial extent, origin, and whole volume between the modern hydrothermal deposits and ancient BIFs, it is unreasonable to compare these features directly. However, our study does provide a miniature but ideal model to dissect the genetic process of BIFs, because the present-day seafloor hydrothermal system could share a series of common characteristics with the ancient Ocean, including the anaerobic environment, higher temperature, the coprecipitation mechanism of Fe-Si oxyhydroxides, or even the possibility of the involvement of chemolithoautotrophic microbes. In this respect, our current results provide yet another means for generating BIFs and thereby warrant additional research.

6. Conclusions

A new hydrothermal field has been discovered on the SWIR, and low-temperature Fe-Si oxyhydroxide deposits have been sampled in order to study the mineralogy and formation there. Based on integrated mineralogical analyses, we have identified a variety of biogenic filamentous structures composed mainly of Fe-Si oxyhydroxide along with abundant of amorphous of opal within these deposits. As revealed by microtexture and previous parallel molecular biological study, neutrophilic FeOB (*Mariprofundus ferrooxydans*) exert a significant role in forming these Fe-rich oxyhydroxides. Our Fourier transform infrared spectroscopy analysis has revealed the presence of a Si-O-Fe bond resulting from the surface binding of Si to Fe-OH functional groups and a Si-O-Si bond representing polymerization of silica in the biogenic mats. These data show that precipitation of silica was only a passive process, whereby ferrihydrite acted as a template for SiO_2. Our study also discovered the alternating microlayer structures in modern low-temperature Fe-Si oxyhydroxide deposits. The Fe-rich layers are mainly a consequence of enzymatic neutrophilic FeOB which are pervasive at the waning stage of hydrothermal activity, whereas the Si-rich layer represents temperature fluctuation in the waxing stage of hydrothermal activity. These findings provide significant implications for the investigation of ancient BIFs: (i) chemolithoautotrophic FeOB could be a tempting explanation for the existence of BIFs, thus expanding the formation environment into wider deep sea rather than long speculated shallow area in ancient oceans and (ii) precipitation of silica may have a close affinity with preformed Fe oxyhydroxide, as indicated by their analogues in modern seafloor hydrothermal vent systems.

Acknowledgments

This study was funded by the National Key Basic Research Program of China (grants 2013CB429701 and 2015CB755905), the National Natural Science Foundation of China (grants 41376077 and 41406067), and the Knowledge Innovation Program of the Chinese Academy of Sciences (SIDSSE-QN-201303). The authors would like to acknowledge Fang Jianyong (Third Institute of Oceanography State Oceanic Administration) for the help with the EPMA, Wen Ling (China University of Petroleum) for her help with the field emission scanning electron microscope and energy-dispersive spectrometer analyses, Jiang Yunshui (Qingdao Institute of Marine Geology) for his help with the X-ray diffraction analysis, and Bao Shenxu (Wuhan University of Technology) for his help with the Fourier transform infrared spectroscopy analysis.

References

Bach, W., N. R. Banerjee, H. J. B. Dick, and E. T. Baker (2002), Discovery of ancient and active hydrothermal systems along the ultra-slow spreading Southwest Indian Ridge 10–16°E, *Geochem. Geophys. Geosyst.*, *3*(7), 1044, doi:10.1029/2001GC000279.

Baker, E. T., and C. R. German (2004), On the global distribution of hydrothermal vent fields, in *Mid-Ocean Ridges: Hydrothermal Interactions Between the Lithosphere and Oceans*, edited by C. R. German, J. Lin, and L. M. Parson, pp. 245–266, AGU, Washington, D. C.

Baker, E. T., G. J. Massoth, R. A. Feely, R. W. Embley, R. E. Thomson, and B. J. Burd (1995), Hydrothermal event plumes from the coaxial seafloor eruption site, Juan de Fuca Ridge, *Geophys. Res. Lett.*, *22*, 147–150, doi:10.1029/94GL02403.

Barghoorn, E. S., and S. A. Tyler (1965), Microorganisms from the Gunflint chert, *Science*, *147*, 563–577.

Beveridge, T. J., and W. S. Fyfe (1985), Metal fixation by bacterial cell walls, *Can. J. Earth Sci.*, *22*, 1983–1989.

Boyd, T. D., and S. D. Scott (2001), Microbial and hydrothermal aspects of ferric oxyhydroxides and ferrosic hydroxides: The example of Franklin Seamount, Western Woodlark Basin, Papua New Guinea, *Geochem. Trans.*, *2*, 45.

Brown, D. A., G. A. Gross, and J. A. Sawicki (1995), A review of the microbial geochemeistry of banded iron-formations, *Can. Mineral.*, *33*, 1321–1333.

Camuti, K. S., and P. T. McGuire (1999), Preparation of polished thinsections from poorly consolidated regolith and sediment materials, *Sediment. Geol.*, *128*, 171–178.

Cannat, M., C. Rommevaux-Jestin, D. Sauter, C. Deplus, and V. Mendel (1999), Formation of the axial relief at the very slow spreading Southwest Indian Ridge (49° to 69°E), *J. Geophys. Res.*, *104*, 22,825–22,843, doi:10.1029/1999JB900195.

Carlson, L., and U. Schwertmann (1981), Natural ferrihydrites in surface deposits from Finland and their association with silica, *Geochim. Cosmochim. Acta*, *45*, 421–429.

Chan, C. S., S. C. Fakra, D. Emerson, E. J. Fleming, and K. J. Edwards (2011), Lithotrophic iron-oxidizing bacteria produce organic stalks to control mineral growth: Implications for biosignature formation, *ISME J.*, *5*, 717–727.

Chen, Y. J., and J. Li (2009), National news: China, *InterRidge News*, *18*, 29–30.

Cloud, P. E. (1973), Paleobiological significance of iron formations, *Econ. Geol.*, *68*, 1135–1143.

Dekov, V. M., and C. Savelli (2004), Hydrothermal activity in the SE Tyrrhenian Sea: An overview of 30 years of research, *Mar. Geol.*, *204*, 161–185.
Dekov, V. M., et al. (2009), Metalliferous sediments from Eolo Seamount (Tyrrhenian Sea): Hydrothermal deposition and re-deposition in a zone of oxygen depletion, *Chem. Geol.*, *264*, 347–363.
Dymek, R. F., and C. Klein (1988), Chemistry, petrology, and origin of banded iron-formation lithologies from the 3800 Ma Isua supracrustal belt, west Greenland, *Precambrian Res.*, *39*, 247–302.
Edwards, K. J., et al. (2011), Ultra-diffuse hydrothermal venting supports Fe-oxidizing bacteria and massive umber deposition at 5000 m off Hawaii, *ISME J.*, doi:10.1038/ismej.2011.48.
Emerson, D., and C. Moyer (1997), Isolation and characterization of novel iron-oxidizing bacteria that grow at circumneutral pH, *Appl. Environ. Microbiol.*, *63*, 4784–4792.
Emerson, D., and C. L. Moyer (2002), Neutrophilic Fe-oxidizing bacteria are abundant at the Loihi Seamount hydrothermal vents and play a major role in Fe oxide deposition, *Appl. Environ. Microbiol.*, *68*, 3085–3093.
Emerson, D., J. A. Rentz, T. G. Lilburn, R. E. Davis, H. Aldrich, C. Chan, and C. L. Moyer (2007), A novel lineage of proteobacteria involved in formation of marine Fe-oxidizing microbial mat communities, *PLoS One*, *2*(7), e667, doi:10.1371/journal.pone.0000667.
Emerson, D., E. J. Fleming, and J. M. McBeth (2010), Iron-oxidizing bacteria: An environmental and genomic perspective, *Annu. Rev. Microbiol.*, *64*, 561–583.
Eugster, H. P., and I. Ming-Chou (1973), The depositional environments of Precambrian banded iron formations, *Econ. Geol.*, *68*, 1144–1168.
Farmer, V. C. (1974), The layer silicates, in *Infrared Spectra of Minerals*, edited by V. C. Farmer, chap. 15, pp. 331–363, Mineralogical Society, London.
Fein, J. B., S. Scott, and N. Rivera (2002), The effect of Fe on Si adsorption by Bacillus subtilis cell walls: Insights into non-metabolic bacterial precipitation of silicate minerals, *Chem. Geol.*, *182*, 265–273.
Fleming, E. J., R. E. Davis, S. M. McAllister, C. S. Chan, C. L. Moyer, B. M. Tebo, and D. Emerson (2013), Hidden in plain sight: Discovery of sheath-forming, iron-oxidizing Zetaproteobacteria at Loihi Seamount, Hawaii, USA, *FEMS Microbiol. Ecol.*, *85*(1), 116–27.
Font, L., B. J. Murton, S. Roberts, and A. G. Tindle (2007), Variations in melt productivity and melting conditions along SWIR (70°E–49°E): Evidence from olivine-hosted and plagioclase-hosted melt inclusions, *J. Petrol.*, *48*(8), 1471–1494.
Fru, E. C., M. Ivarsson, S. P. Kilias, S. Bengtson, V. Belivanova, F. Marone, D. Fortin, C. Broman, and M. Stampanoni (2013), Fossilized iron bacteria reveal a pathway to the biological origin of banded iron formation, *Nat. Commun.*, *4*, 2050, doi:10.1038/ncomms3050.
Fujimoto, H., et al. (1999), First submersible investigations of mid-ocean ridges in the Indian Ocean, *InterRidge News*, *8*, 22–24.
Georgen, J. E., J. Lin, and H. J. B. Dick (2001), Evidence from gravity anomalies for interactions of the Marion and Bouvet hotspots with the Southwest Indian Ridge: Effects of transform offsets, *Earth Planet. Sci. Lett.*, *187*, 283–300.
German, C. R. (2003), Hydrothermal activity on the eastern Southwest Indian Ridge (50°–70°E): Evidence from core-top geochemistry, 1887 and 1998, *Geochem. Geophys. Geosyst.*, *4*(7), 9102, doi:10.1029/2003GC000522.
German, C. R., and L. M. Parson (1998), Distributions of hydrothermal activity along the mid-Atlantic ridge: Interplay of magmatic and tectonic control, *Earth Planet. Sci. Lett.*, *160*, 327–341.
Gloter, A., M. Zbinden, F. Guyot, F. Gaill, and C. Colliex (2004), TEM-EELS study of natural ferrihydrite from geological-biological interactions in hydrothermal systems, *Earth Planet. Sci. Lett.*, *222*, 947–957.
Golubic, S., and S. J. Lee (1999), Early cyanobacterial fossil record: Preservation, palaeoenvironments, and identification, *Eur. J. Phycol.*, *34*, 339–348.
Grenne, T., and J. F. Slack (2003), Bedded jaspers of the Ordovician Lokken ophiolite, Norway: Seafloor deposition and diagenetic maturation of hydrothermal plume-derived silica-iron gels, *Miner. Deposita*, *38*, 625–639.
Guidry, S. A., and H. S. Chafetz (2002), Factors governing subaqueous siliceous sinter precipitation in hot springs: Examples from the Yellowstone National Park, USA, *Sedimentology*, *49*, 1253–1267.
Holland, H. D. (1973), The oceans: A possible source of iron in iron formations, *Econ. Geol.*, *68*, 1169–1172.
Holm, N. G. (1987a), Biogenic influences on the geochemistry of certain ferruginous sediments of hydrothermal origin, *Chem. Geol.*, *63*, 45–57.
Holm, N. G. (1987b), Possible biological origin of banded iron formations from hydrothermal solutions, *Origins Life*, *17*, 229–250.
Hrischeva, E., and S. D. Scott (2007), Geochemistry and morphology of metalliferous sediments and oxyhydroxides from the Endeavour segment, Juan de Fuca Ridge, *Geochim. Cosmochim. Acta*, *71*, 3476–3497.
Jones, B., K. O. Konhauser, R. W. Renaut, and R. S. Wheeler (2004), Microbial silicification in Iodine Pool, Waimangu geothermal area, North Island, New Zealand: Implications for recognition and identification of ancient silicified microbes, *J. Geol. Soc.*, *161*, 983–993.
Juniper, S. K., and Y. Fouquet (1988), Filamentous iron-silica deposits from modern and ancient hydrothermal sites, *Can. Mineral.*, *26*, 859–869.
Kappler, A., C. Pasquero, K. O. Konhauser, and D. K. Newman (2005), Deposition of banded iron formations by anoxygenic phototrophic Fe(II)-oxidizing bacteria, *Geology*, *33*, 865–868.
Kato, S., C. Kobayashi, T. Kakegawa, and A. Yamagishi (2009), Microbial communities in iron-silica-rich microbial mats at deep-sea hydrothermal fields of the Southern Mariana Trough, *Environ. Microbiol.*, *11*, 2094–2111.
Kennedy, C. B., R. E. Martinez, S. D. Scott, and F. G. Ferris (2003a), Surface chemistry and reactivity of bacteriogenic iron oxides from Axial Volcano, Juan de Fuca Ridge, north-east Pacific Ocean, *Geobiology*, *1*, 59–69.
Kennedy, C. B., S. D. Scott, and F. G. Ferris (2003b), Characterization of bacteriogenic iron oxide deposits from Axial Volcano, Juan de Fuca Ridge, north-east Pacific Ocean, *Geomicrobiol. J.*, *20*, 199–214.
Kennedy, C. B., S. D. Scott, and F. G. Ferris (2004), Hydrothermal phase stabilization of two-line ferrihydrite by bacteria, *Chem. Geol.*, *212*, 269–277.
Koji, N., and P. H. Solomon (1977), *Infrared Adsorption Spectroscopy*, Holden-Day, Inc., San Francisco, Calif.
Konhauser, K. O., B. Jones, V. R. Phoenix, G. Ferris, and R. W. Renaut (2004), The microbial role in hot spring silicification, *Ambio*, *33*, 552–558.
Kukkadapu, R. K., J. M. Zachara, J. K. Fredrickson, and D. W. Kennedy (2004), Biotransformation of two-line silica-ferrihydrite by a dissimilatory Fe(III)-reducing bacterium: Formation of carbonate green rust in the presence of phosphate, *Geochim. Cosmochim. Acta*, *68*, 2799–2814.
Landmesser, H., H. Kosslick, W. Storek, and R. Fricke (1997), Interior surface hydroxyl groups in ordered mesoporous silicates, *Solid State Ionics*, *271*, 101–103.
Lazarev, A. N. (1972), *Vibrational Spectra and Structure of Silicates*, pp. 123–124, Plenum Press, New York.
Li, J. W., X. T. Peng, H. Y. Zhou, J. T. Li, and Z. L. Sun (2013), Molecular evidence for microorganisms participating in Fe, Mn, and S biogeochemical cycling in two low-temperature hydrothermal fields at the Southwest Indian Ridge, *J. Geophys. Res. Biogeosci.*, *118*, 665–679, doi:10.1002/jgrg.20057.

Li, Y.-L. (2014), Micro- and nanobands in late Archean and Palaeoproterozoic banded-iron formations as possible mineral records of annual and diurnal depositions, *Earth Planet. Sci. Lett.*, *391*, 160–170.
Little, C. T. S., T. Danelian, R. J. Herrington, and R. M. Haymon (2004), Early Jurassic hydrothermal vent community from the Franciscan Complex, California, *J. Paleontol.*, *78*, 542–559.
Massoth, G. J., E. T. Baker, J. E. Lupton, R. A. Feely, D. A. Butterfield, K. Von Damm, K. K. Roe, and G. T. Lebon (1994), Temporal and spatial variability of hydrothermal manganese and iron at Cleft segment, Juan de Fuca Ridge, *J. Geophys. Res.*, *99*, 4905–4923, doi:10.1029/93JB02799.
Massoth, G. J., E. T. Baker, R. A. Feely, J. E. Lupton, R. E. Collier, J. E. Gendron, K. K. Roe, S. M. Maenner, and J. A. Resing (1998), Manganese and iron in hydrothermal plumes resulting from the 1996 Gorda Ridge Event, *Deep Sea Res., Part II*, *45*, 2683–2712.
Morris, R. C. (1993), Genetic modelling for banded iron-formation of the Hamersley Group, Pilbara Cration, Western Australia, *Precambrian Res.*, *60*, 243–286.
Muller, M. R., T. A. Minshull, and R. White (1999), Segmentation and melt supply at the Southwest Indian Ridge, *Geology*, *27*, 867–870.
Münch, U., C. Lalou, P. Halbach, and H. Fujimoto (2001), Relict hydrothermal events along the super-slow Southwest Indian spreading ridge near 63°56′E: Mineralogy, chemistry, and chronology of sulfide samples, *Chem. Geol.*, *177*, 341–349.
Parenteau, M. N., and S. L. Cady (2010), Microbial biosignatures in iron-mineralized phototrophic mats at Chocolate Pots hot spring, Yellowstone National Park, United States, *Palaios*, *25*, 97–111.
Parfitt, R. L., S. J. Van der Gaast, and C. W. Childs (1992), A structural model for natural siliceous ferrihydrite, *Clays Clay Miner.*, *40*, 675–681.
Pecoits, E., M. K. Gingras, M. E. Barley, A. Kappler, N. R. Posth, and K. O. Konhauser (2009), Petrography and geochemistry of the Dales Gorge banded iron formation: Paragenetic sequence, source, and implications for palaeo-ocean chemistry, *Precambrian Res.*, *172*, 163–187.
Peng, X. T., S. Chen, H. Y. Zhou, L. X. Zhang, Z. J. Wu, J. T. Li, J. W. Li, and H. C. Xu (2011), Diversity of biogenic minerals in low-temperature Si-rich deposits from a newly discovered hydrothermal field on the ultraslow spreading Southwest Indian Ridge, *J. Geophys. Res.*, *116*, G03030, doi:10.1029/2011JG001691.
Planavsky, N., O. Rouxel, A. Bekker, R. Shapiro, P. Fralick, and A. Knudsen (2009), Iron-oxidizing microbial ecosystems thrived in late Paleoproterozoic redox-stratified oceans, *Earth Planet. Sci. Lett.*, *286*, 230–242.
Pokrovski, G. S., J. Schott, F. Farges, and J.-L. Hazemann (2003), Iron (III)-silica interactions in aqueous solution: Insights from X-ray absorption fine structure spectroscopy, *Geochim. Cosmochim. Acta*, *67*, 3559–3573.
Posth, N. R., F. Hegler, K. O. Konhauser, and A. Kappler (2008), Alternating Si and Fe deposition caused by temperature fluctuations in Precambrian oceans, *Nat. Geosci.*, *1*, 703–708.
Rancourt, D. G., D. Fortin, T. Pichler, P.-J. Thibault, G. Lamarche, R. V. Morris, and P. H. J. Mercier (2001), Mineralogy of a natural As-rich hydrous ferric oxide coprecipitate formed by mixing of hydrothermal fluid and sea water: Implications regarding surface complexation and color banding in ferrihydrite deposits, *Am. Mineral.*, *86*, 834–851.
Rentz, J., C. Kraiya, G. Luther III, and D. Emerson (2007), Control of ferrous iron oxidation within circumneutral microbial iron mats by cellular activity and autocatalysis, *Environ. Sci. Technol.*, *41*, 6084–6089.
Rodgers, K. A., et al. (2004), Silica phases in sinters and residues from geothermal fields of New Zealand, *Earth Sci. Rev.*, *66*, 1–61.
Sauter, D., P. Patriat, C. Rommevaux-Jestin, M. Cannat, A. Briais, and Gallieni Shipboard Scientific Party (2001), The Southwest Indian Ridge between 49°15′E and 57°E: Focused accretion and magma redistribution, *Earth Planet. Sci. Lett.*, *192*, 303–317, doi:10.1016/S0012-821X(01)00455-1.
Sauter, D., H. Carton, V. Mendel, M. Munschy, C. Rommevaux-Jestin, J. Schott, and H. Whitechurch (2004), Ridge segmentation and the magnetic structure of the Southwest Indian Ridge (at 50°30′E, 55°30′E and 66°20′E): Implications for magmatic processes at ultraslow-spreading centers, *Geochem. Geophys. Geosyst.*, *5*, Q05K08, doi:10.1029/2003GC000581.
Siever, R. (1992), The silica cycle in the Precambrian, *Geochim. Cosmochim. Acta*, *56*, 3265–3272.
Simonson, B. M. (1985), Sedimentological constraints on the origins of Precambiran iron formations, *Geol. Soc. Am. Bull.*, *96*, 244–252.
Strother, P. K., and K. Tobin (1987), Observations on the genus *Huroniospora barghoorn*: Implications for Paleoecology of the gunflint microbiota, *Precambrian Res.*, *36*, 323–333.
Sun, Z., G. P. Glasby, Q. Yang, X. Yin, J. Li, and Z. Chen (2012), Formation of Fe-Mn-Si oxide and nontronite deposits: Examples from hydrothermal fields on the Valu Fa Ridge, Lau Basin, *J. Asian Earth Sci.*, *43*, 64–76.
Sun, Z., H. Zhou, G. P. Glasby, Z. Sun, X. Yin, and J. Li (2013), Mineralogical characterization and formation of Fe-Si oxyhydroxide deposits from modern seafloor hydrothermal vents, *Am. Mineral.*, *98*, 85–97.
Suzuki, T., H. Hashimoto, N. Matsumoto, M. Furutani, H. Kunoh, and J. Takada (2011), Nanometer-scale visualization and structural analysis of the inorganic/organic hybrid structure of Gallionella ferruginea twisted stalks, *Appl. Environ. Microbiol.*, *77*, 2877–2881.
Swedlund, P. J., and J. G. Webster (1999), Adsorption and polymerization of silicic acid on ferrihydrite and its effect on arsenic adsorption, *Water Res.*, *33*, 3413–3422.
Tamura, H., K. Goto, and M. Nagayama (1976), The effect of ferric hydroxide on the oxygenation of ferrous ions in neutral solutions, *Corros. Sci.*, *16*, 197–207.
Tao, C., et al. (2007), Discovery of the first active hydrothermal vent field at the ultraslow spreading Southwest Indian Ridge: The Chinese DY115219 Cruise, *InterRidge News*, *16*, 25–26.
Tao, C., et al. (2009), New hydrothermal fields found along the Southwest Indian Ridge during the Legs 5–7 of the Chinese DY115–20 expedition Abstract OS21A–1150 presented at AGU Fall Meeting, Eos Transactions supplement.
Tao, C., et al. (2012), First active hydrothermal vents on an ultraslow-spreading center: Southwest Indian Ridge, *Geology*, *40*, 47–50.
Tobler, D. J., A. Stefánsson, and L. G. Benning (2008), In-situ grown silica sinters in Icelandic geothermal areas, *Geobiology*, *6*, 481–502.
Toner, B. M., C. M. Santelli, M. A. Marcus, R. Wirth, C. S. Chan, T. McCollom, W. Bach, and K. J. Edwards (2009), Biogenic iron oxyhydroxide formation at mid-ocean ridge hydrothermal vents: Juan de Fuca Ridge, *Geochim. Cosmochim. Acta*, *73*, 388–403.
Toner, B. M., T. S. Berquó, F. M. Michel, J. V. Sorensen, A. S. Templeton, and K. J. Edwards (2012), Mineralogy of iron microbial mats from Loihi Seamount, *Front. Microbiol.*, *3*, 118, doi:10.3389/fmicb.2012.00118.
Treguer, P., D. M. Nelson, A. J. Van Bennekom, D. J. DeMaster, A. Leynaert, and B. Queguiner (1995), The silica balance in the world ocean: A reestimate, *Science*, *268*, 375–379.
Vempati, R. K., and R. H. Loeppert (1989), Influence of structural and adsorbed Si on the transformation of synthetic ferrihydrite, *Clays Clay Miner.*, *37*, 273–279.
Vempati, R. K., R. H. Loeppert, H. Sittertz-Bhatkar, and R. C. Burghardt (1990), Infrared vibrations of hematite formed from aqueous- and dry-thermal incubation of Si-contanining ferrihydrite, *Clays Clay Miner.*, *38*, 294–298.
Widdel, F., S. Schnell, S. Heising, A. Ehrenreich, B. Assmus, and B. Schink (1993), Ferrous iron oxidation by anoxygenic phototrophic bacteria, *Nature*, *362*, 834–836.

Yee, N., V. R. Phoenix, K. O. Konhauser, L. G. Benning, and F. G. Ferris (2003), The effect of cyanobacteria on silica precipitation at neutral pH: Implications for bacterial silicification in geothermal hot springs, *Chem. Geol.*, *199*, 83–90.

Ying, F., Y. Shui-li, Y. Yan-zhen, Q. Li-ping, and H. Ban (2007), Reaction mode between Si and Fe and evaluation of optimal species in poly-silicic-ferric coagulant, *J. Environ. Sci.*, *19*, 678–688.

Zhao, J., F. E. Huggins, Z. Feng, and G. P. Huffman (1994), Ferrihydrite: Surface structure and its effects on phase transformation, *Clays Clay Miner.*, *42*, 737–746.

Zhu, J., J. Lin, Y. J. Chen, C. Tao, C. R. German, D. R. Yoerger, and M. A. Tivey (2010), A reduced crustal magnetization zone near the first observed active hydrothermal vent field on the Southwest Indian Ridge, *Geophys. Res. Lett.*, *37*, L18303, doi:10.1029/2010GL043542.